



An investigation of photoelectrocatalytic disinfection of water using titania nanotube photoanodes with carbon cathodes and determination of the radicals produced

S. McMichael^{*}, A. Tolosana-Moranchel, M.A.L.R.M. Cortes, J.W.J. Hamilton, P. Fernandez-Ibanez, J.A. Byrne^{*}

NIBEC, Ulster University, Newtownabbey BT37 0QB, United Kingdom

ARTICLE INFO

Keywords:

TiO₂ nanotubes
Photoelectrocatalysis
Platinum nanoparticles
Cathode
Gas diffusion electrode

ABSTRACT

In photoelectrocatalysis (PEC) a considerable amount of research has been focused on improving the photo-electrode; however, cathodic reactions are essential to PEC disinfection. In this work, a TiO₂ nanotube (TiNT) array was used as the photoanode with various cathode electrodes materials, including gas diffusion electrodes (GDE) modified with different Pt nanoparticle loadings. The highest rate of *E. coli* inactivation was achieved with the non-modified GDE (2.51 log) compared to Pt mesh paddle (0.79 log reduction). This was explained by the examining reactive oxygen species generated at the counter electrode, where the non-modified GDE had the highest Faradaic efficiency of 15.5% for the formation of H₂O₂. Modification with Pt inhibited the formation of H₂O₂ to below the detection limit. The TiNT photoanode was shown to generate hydroxyl radicals, but importantly, there was reduction of molecular oxygen to superoxide radical at the anode. A thin cell reactor was then constructed using the identified optimal materials and a 5.0 log reduction in *E. coli* was in 20 min under UVA irradiation.

1. Introduction

Photoelectrocatalysis (PEC) is commonly conducted with an n-type photoanode and a conducting counter electrode with an externally applied bias; a diagram of this process is shown in Fig. 1. The photo-electrode (left Fig. 1) can absorb photons with energy greater than the bandgap (E_g) resulting in the generation of an electron (e^-) and hole (h^+) pair. Under an applied bias, conduction band electrons move via the external circuit to the counter electrode, thereby separating electron hole pairs and reducing the rate of charge carrier recombination [1]. Overall, this results in reduction and oxidation reactions occurring at spatially separated electrodes.

Titanium dioxide nanotube (TiNT) photoanodes have been reported to be effective for the inactivation of microorganisms [2–4]. Recent research progress using TiNT has been summarised in reviews [5,6]. Other progress includes the design of PEC reactor with a compound parabolic collector, tested under real solar irradiation during winter in South Africa for inactivation of environmental strains of bacteria [7].

Other work has investigated the modification of TiNTs with γ -graphene [8], formation of WO₃ heterostructures [9] and doping with N₂ [10]. The latter improved the inactivation rate for *E. coli*, despite a lower current density for the doped samples, demonstrating that the rate of disinfection is not directly proportional to the photocurrent when comparing different photoanodes. It was suggested that the type of ROS generated had a greater influence on the rate of disinfection and the generation of superoxide ($O_2^{\bullet-}$) at the photoanode could be responsible for the improved disinfection rate, although this was not proven experimentally. As such, in this paper the detection and quantification of the ROS species, $O_2^{\bullet-}$ & hydroxyl radical ($\bullet OH$) was performed at the photoanode.

In PEC less analysis has been performed on the selection of the counter electrode material for generating reactive oxygen species (ROS). The complete oxygen reduction reaction (ORR) is the 4 electrons reduction to water (Eq. 1 and 2) [11]. This reaction is not beneficial when applied to PEC for water treatment or disinfection; instead, the

^{*} Corresponding authors.

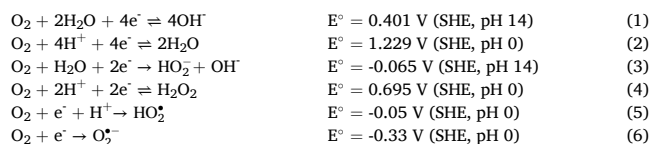
<https://doi.org/10.1016/j.apcatb.2022.121339>

Received 13 November 2021; Received in revised form 4 March 2022; Accepted 19 March 2022

Available online 23 March 2022

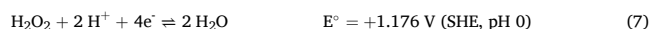
0926-3373/© 2022 The Authors. Published by Elsevier B.V. This is an open access article under the CC BY-NC-ND license (<http://creativecommons.org/licenses/by-nc-nd/4.0/>).

desirable ORR are one's which produce ROS (represented in Eqs. 3–6).



Several different counter electrodes are reported for PEC reactors, such as Ti [12–14], nickel [15,16], stainless steel [17,18], carbon-based materials [4,19,20], and Pt which is the most commonly used owing to its high electrochemical stability and catalytic activity [3,10,21–25]. However, the suitability of Pt in PEC is limited due to cost, but also has implications for the desired reduction reaction, therefore an examination of Pt counter electrodes for PEC disinfection is required. The use of nanoparticles (NP) may offer a lower-cost method by reducing the amount of Pt required, as such investigations using Pt NP are also examined in this paper.

It has been reported that there is a synergistic effect on the inactivation of *Escherichia coli* (*E. coli*) with low levels of H_2O_2 and UVA irradiation [26,27]; therefore, the generation of H_2O_2 is expected to enhance the overall process. The generation of H_2O_2 with carbon-based electrodes has been reported by Ma et al. [28] who examined the use of carbon felt with 50 mM Na_2SO_4 adjusted to pH 3 with sulphuric acid and at -0.9 V (SCE) generating the highest concentration of H_2O_2 . Depending on the experimental set up the H_2O_2 generation efficiency changed over time due to further cathodic reduction (Eq. 7) and anodic oxidation (Eq. 4) of the generated H_2O_2 . Optimal current density and applied potential, a higher cathode area than anode were shown to improve efficiency, as too does mixing and the type of anode used.



Barros et al. [29] used an unmodified carbon gas diffusion electrode (GDE) in a single-cell reactor and achieved a Faradaic efficiency of 33.3% at -1.1 V (Ag/AgCl) though it was conducted at pH 14. Zhang et al. [30] modified a GDE with PTFE to produce a hydrophobic surface with a carbon black catalyst. The use of the GDE removes the need to sparge the electrolyte with air or oxygen. They reported 64.9%

efficiency for the formation of H_2O_2 in 50 mM Na_2SO_4 adjusted to pH 3 (H_2SO_4). The electrochemical generation of H_2O_2 is commonly conducted at pH values outside of the range of natural water sources (6.5–8.5 [31]). Therefore, examination of suitable counter electrodes at neutral pH is required.

In this work oxygen reduction products were assessed at different counter electrode materials including Pt wire, carbon felt, carbon GDE and carbon GDE modified with Pt nanoparticles. The formation of $\bullet OH$ & $O_2^{\bullet -}$ were examined at the photoanode. The photoelectrochemical properties of TiNT on Ti foil and Ti mesh were also determined. The combination of the photoanode with different counter electrodes in a PEC was investigated for the inactivation of *E. coli* K12. The optimal materials were then incorporated into a custom design PEC for disinfection experiments using local stream water under UVA irradiation.

2. Experimental section

2.1. Materials

The materials and chemicals used are as follows: ammonium fluoride (Sigma-Aldrich $\geq 99.99\%$), carbon paper (Ion-power), carbon felt (Alfa Aesar), chloroplatinic acid (Sigma-Aldrich $\geq 99.9\%$), conductive epoxy CW 2400 (Circuit works), copper sheet & wire (RS Components), Coumarin (Sigma-Aldrich $\geq 99\%$), Decon 90 (Decon Laboratories), ethylene glycol (Sigma-Aldrich $\geq 99\%$), hydrogen peroxide (Sigma-Aldrich 30%), hydroquinone (Sigma-Aldrich $\geq 99\%$), nitrogen (oxygen-free) (BOC $\geq 99.99\%$), palatium wire (Birmingham metal special products), potassium chloride (Sigma Aldrich $\geq 99.0\%$), potassium iodide (Sigma Aldrich $\geq 99.0\%$), ringer's solution ¼ strength tablets (Fluka Analytical), sodium bicarbonate (Sigma-Aldrich $\geq 99.7\%$), sodium chloride (Sigma-Aldrich $\geq 99.8\%$), sodium sulphate (Sigma-Aldrich $\geq 99.0\%$), titanium foil (Sigma-Aldrich 99.80%), titanium mesh (Ti-Shop Grade I), trypticase soy agar (Sigma-Aldrich), trypticase soy broth (Sigma-Aldrich), umbelliferone (Sigma-Aldrich 99.0%), UV grade acrylic (Plasticstockist.com).

2.2. Electrodeposition of platinum nanoparticles on GDE

Platinum nanoparticles were electrodeposited onto the GDE in a 3 electrode electrochemical cell with the GDE as the working electrode, Pt mesh counter and saturated calomel reference (SCE) with 5 mM H_2PtCl_6 in 0.5 M H_2SO_4 electrolyte [32]. The electrodeposition was conducted in a custom-built cell (Fig. S1).

The electrodeposition was performed in 2 steps, first a potential of

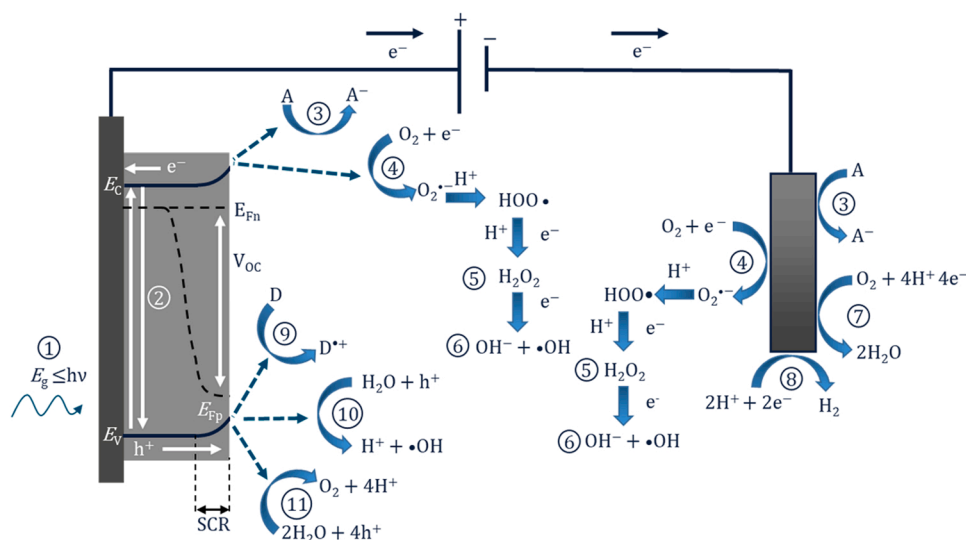


Fig. 1. Diagram of the PEC process and pathways for radical production using a photoanode and a non-semiconducting counter electrode. 1) Photon absorption, 2) photo-excitation and recombination, 3) electron transfer to an electron acceptor, 4) oxygen reduction to superoxide, 5) formation of hydrogen peroxide, 6) formation of hydroxyl radical, 7) oxygen and proton reduction to water, 8) proton reduction to hydrogen, 9) donor electron transfer, 10) oxidation of water to form a hydroxyl radical, 11) oxygen evolution reaction. (Adapted with permission from [1] (MDPI Basel, Switzerland)).

– 0.5 V (SCE) for 5 s was applied for all samples and second a potential of 0.0 V (SCE); with different applied durations of 10 s, 20 s, 40 s, & 80 s to vary the amount of Pt on the GDE. Accordingly, the samples are labelled as GDE (no modification), Pt 10 s, Pt 20 s, etc. A scanning electron microscope (Hitachi SU5000 FE-SEM) was then used to image the Pt NT. The software “ImageJ” was then used to calculate the cross-sectional area and diameter of the nanoparticles using the built-in “Analyze Particles” function with a threshold image [33]. The SEM was equipped with an energy dispersive X-ray (EDX/EDS) analyser and conducted with an accelerating voltage of 7.5 kV. The images were recorded with a backscattered secondary electron detector and performed with the Aztec software provided with the instrument, to confirm the nanoparticles were Pt.

2.3. Oxygen reduction

To assess the efficiency for oxygen reduction, linear sweep voltammetry (LSV) was used. A 3-electrode configuration using a custom-made single cell (Fig. S1), with 2 cm² exposed for the cathode (working electrode) which also enabled air purging through the porous electrodes. The electrolyte was 0.1 M KCl, the reference electrode was a SCE and a platinum mesh paddle (5.9 cm²) anode. The electrodes were connected to an electrochemical workstation (AUTOLAB PGSTAT 30) LSV was used from + 0.5 V to – 1.5 V at a rate of 5 mVs^{–1}. To remove the oxygen from the electrolyte, oxygen-free nitrogen was used to purge the cell for 10 min before running the scan and N₂ blanketing during the scan. For oxygen reduction, air purging was performed using a peristaltic pump (Pharmacia LKB) for 10 min before running the scan. The materials examined were, platinum wire, carbon felt, GDE non-hydrophobic side, GDE hydrophobic side, GDE hydrophobic side with platinum deposited via differing cycle times Pt 10 s, Pt 20 s, Pt 40 s & Pt 80 s

2.4. Hydrogen peroxide quantification

To examine the amount of H₂O₂ generated, titanium oxysulfate was used as a colorimetric detection method [34] which produces a yellow complex in the presence of H₂O₂. A calibration curve was produced (Fig. S2) using 2 mL of 280 mM of titanium oxysulfate in dilute sulphuric acid and 1 mL solution. The solutions of H₂O₂ (1, 5, 10, 20 mg L^{–1}) were prepared by serial dilutions of 30% H₂O₂ (Sigma-Aldrich) using de-ionised water. The absorption was measured using a Jenway 6305 spectrophotometer with a fixed wavelength of 410 nm. The cathodes were tested with a Pt mesh paddle (5.9 cm²) counter electrode, a SCE reference electrode operated at – 0.75 V, in a solution of 0.1 M KCl. Additional experiments were conducted using the highest Pt loading (Pt 80 s) with different potentials/electrolytes (Table S1).

2.5. Anodisation of titanium

All titanium (Ti) samples were cut into segments and ultrasonically cleaned in a solution of 5% Decon 90 detergent, followed by washing in distilled water to remove any Decon 90 and finally dried in air. The Ti was anodised following the method reported by Yeonmi et al. [35]. In brief, a two-electrode cell was used with the sample (Ti) as the working electrode and 2 Ti mesh as the cathodes on either side of the working electrode. The electrolyte solution contained NH₄F (0.3 wt%) in distilled water (3 vol%) and ethylene glycol (97 vol%). This was conducted in a polypropylene beaker at +30.0 V (PLH120 DC power supply from Aim-TTi) for 3 h, then rinsed multiple times in distilled water. Two different annealing temperatures were used at 350 °C and 450 °C. Confirmation nanotube growth and morphological analysis was performed by using SEM (Hitachi SU5000 FE-SEM). A contact area on the Ti was cleaned using abrasive paper and an electrical contact was made by attaching a copper wire to the Ti that had been cleaned using silver epoxy (CircuitWorks CW2400). To insulate the contact and ensure that a 1.0 × 1.0 cm photoactive area was exposed for the

photoelectrochemical measurements, a negative SU8 photoresist (MicroChem) was applied and left to dry at room temperature. Once dry, the coated photoelectrode was exposed to UVA (PL-S 9 W/10/2 P (UVA)) for 5 min on both sides to enable the cross-linking of the epoxy groups, followed by curing in an oven at 160 °C for 30 min. Titanium mesh was also used as an anode material. The wire mesh had a 0.2 mm diameter with an open area of 52.48%. As the open area of the mesh limits the absorption area, multiple meshes were layered on top of one another (Fig. S3). The opening area can be calculated using Eq. 8, where A_o is the open area (%), w is the depth (mm), m is the number of meshes, η (between 0 and 1) can be used to account for miss alignment and d is the diameter of the mesh wire (mm). Consequently, 3 meshes were layered on top of each other to form a photoelectrode, resulting in an open area of 2% (provided 100% alignment i.e. η = 1). By using multiple meshes there is an increase in the geometric surface area (Table S2), as such photoelectrochemical measurements of the meshes are defined as, “normalised current density” to signify that area irradiated is 1.0 × 1.0 cm.

$$A_o = \left(\frac{w - ((m-1)\eta d)}{w + d} \right)^2 \quad w \geq ((m-1)\eta d) \geq 0 \quad (8)$$

2.6. Photoelectrochemical analyses of photoelectrodes

To examine the photoelectrochemical properties of the photoelectrode, a three-electrode single cell compartment (Fig. S4) was used. The working photoelectrode (1 × 1 cm exposed segment), a platinum mesh paddle (5.9 cm²) counter electrode and a SCE as the reference electrode. The irradiance source was a 450 W Xe lamp (Horiba Jobin Yvon FL-1039/40) which had an intensity of 343.2 Wm^{–2} between 270 and 800 nm and 21.3 Wm^{–2} between 270 and 400 nm; it was also equipped with a monochromator (Horiba Jobin Yvon MicroHR) spectrum shown in Figs. S5 and S6. The incident photon conversion efficiency (IPCE) was calculated using Eq. 9, where I is the current (A), t is the time (s), e is the number of electrons in a coulomb (6.24 × 10¹⁸), A is the area of the photoelectrode (cm²) and P_λ is photon density per second (photons cm^{–2} s^{–1}) for a set wavelength. The electrodes were connected to an electrochemical workstation (AUTOLAB PGSTAT 30) and controlled by a PC using General Purpose Electrochemical Software (GPES). All photoelectrochemical analyses experiments were carried out in 0.1 M KCl to be consistent with the oxygen reduction experiments. To examine the change in photocurrent for different UV intensity, a 1000 W Xe lamp was used with the reactor positioned at various positions from the lamp to vary the UV intensity.

$$\text{IPCE} = \frac{\text{number of charge carriers generated}}{\text{number of incident photons}} = \frac{I t e}{t A \int P_{\lambda} d\lambda} \quad (9)$$

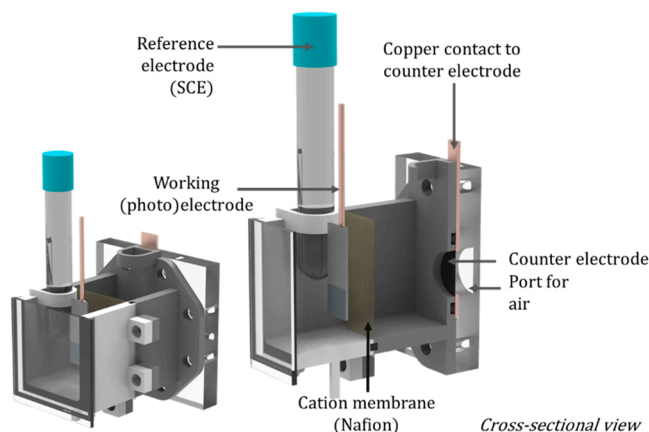


Fig. 2. Two-compartment reactor for radical detection at the photoanode.

2.7. Hydroxyl radical detection

To detect and quantify the amount of hydroxyl radicals ($\bullet\text{OH}$) generated, a two-compartment cell (Fig. 2) with magnetic stirring was used. The compartments were separated by a cation membrane (Nafion) to prevent interference with the working electrode. The cell was operated as a 3-electrode set-up in 0.1 M KCl electrolyte, the working electrode was the photoelectrode being examined, the counter electrode was a carbon paper counter electrode, and the reference was SCE.

Coumarin (0.4 mM) was used as the probe to detect $\bullet\text{OH}$ as reported by [36]. Due to the low solubility and dissolution speed of coumarin, it was dissolved at elevated temperatures [37]. The reaction of coumarin and $\bullet\text{OH}$ (Fig. S7) results in the formation of 7-hydroxycoumarin (also known as Umbelliferone), the latter can be detected by fluorescence's i. e. a rise in the fluorescence indicates the generation of $\bullet\text{OH}$.

The quantification of 7-hydroxycoumarin was performed using an Agilent Cary Eclipse fluorescence spectrophotometer with a quartz cuvette and 2 mL of sample. A calibration curve (Fig. S8) was produced by using a known concentration of 7-hydroxycoumarin dissolved under magnetic stirring at elevated temperatures in 0.1 M KCl. Serial dilutions were performed to adjust the concentration. The excitation wavelength used was $\lambda_{\text{ex}} = 332 \text{ nm}$ and the peak emission wavelength $\lambda_{\text{em}} = 456 \pm 3 \text{ nm}$.

2.8. Superoxide detection

To detect and quantify superoxide ion radicals ($\text{O}_2^{\bullet-}$) at the photoanode, the two-compartment cell (Fig. 2) as previously described was used. The solution was 0.1 M KCl, the $\text{O}_2^{\bullet-}$ scavaging probe was 0.2 mM 1,4-hydroquinone reported by Fónagy et al. [38] which was reported to be more selective towards $\text{O}_2^{\bullet-}$ than benzoquinone. Potassium iodide (5 mM) was used as a hole and $\bullet\text{OH}$ scavenger to prevent possible oxidation of hydroquinone [39,40]. N_2 purging was used to remove oxygen from the solution for control experiments. The reaction of $\text{O}_2^{\bullet-}$ and hydroquinone (H_2Q) forms benzosemiquinone radical (BQH^\bullet) and hydrogen peroxide (Eq. 10) [41].



The detection and qualification of hydroquinone were performed by using a fluorescence spectrophotometer (Agilent Cary Eclipse) with a quartz cuvette and 2 mL of sample. A calibration curve (Fig. S9) was produced by using a known concentration of hydroquinone, serial dilutions were performed to adjust the concentration. The excitation wavelength was $\lambda_{\text{ex}} = 288 \text{ nm}$ and the peak emission wavelength $\lambda_{\text{em}} = 330 \text{ nm}$.

2.9. *E. coli* K12 inactivation experiments

The inactivation of *E. coli* K12 was conducted in a custom-made cell (Fig. S10), with a 2 cm^2 GDE counter electrode and $1.0 \times 1.0 \text{ cm}^2$ photoanode, with a working volume of 15 mL giving a surface to volume ratio of $0.067 \text{ cm}^2 \text{ cm}^{-3}$. A UVA lamp was used for the inactivation experiments (365 nm with 30.9 W m^{-2}) and a cell potential used (PLH120 DC power supply from Aim-TTi) as both can be easily developed into a working reactor design in the future. Between each run, the reactor was cleaned with 3% vol H_2O_2 and rinsed with deionised water 4 times to remove any residual H_2O_2 . The use of a chloride electrolyte (60 mM NaCl) was firstly examined for the inactivation of *E. coli* but to remove the complication of chlorine species [42], 60 mM Na_2SO_4 was used as the aim of this work was to investigate the formation of ROS. The different experiments conducted are stated in Table S3.

2.10. Thin cell reactor

To examine the influence of the surface area to volume ratio, a thin

cell reactor was tested (Fig. S11) which had a surface-to-volume ratio of $2.01 \text{ cm}^2 \text{ cm}^{-3}$ and tested under the same parameters as before, i.e. 60 mM of Na_2SO_4 , GDE (non-modified), TiNT mesh annealed at 350°C , operated at $+1.0 \text{ V}$ though with a slightly lower intensity of 24.7 W m^{-2} (365 nm peak) due to the positioning. The effect of a higher irradiance (45.6 W m^{-2}) was subsequently examined, as too was the disinfection using natural autoclaved stream water.

Stream water was collected from a local source using a washed and autoclaved glass bottle (Schott). The stream water was then autoclaved to inactivate any naturally present microorganisms. Selected parameters of the stream water before and after autoclaving are stated in Table 1. The stream water was then stored in a fridge ($2-8^\circ\text{C}$) until testing and spiked with *E. coli* K12 as previously described and plated following the same procedure.

2.11. Microbially culture & analyses

A stock plate of *E. coli* K12 (NCTC 12486) was prepared using lyophilised strains. The lyophilised sample was taken from a freezer and a fresh culture was prepared using tryptic soy broth (TSB) inoculated with 2 lyophilised bacteria spheres and incubated at 37°C for 21 h under constant agitation of 120 rpm in an orbital rotary shaker; producing a concentration of $> 10^9$ colony-forming units (CFU) mL^{-1} . Serial dilutions were performed using $\frac{1}{4}$ strength Ringers solutions and 100 μL spread plated on tryptic soy agar (TSA) and incubated 37°C for 24 h. The plate with a suitable number of colonies (75–200) was used as the stock plate.

The electrolyte solution to be used in the reactor was spiked with the required volume of stock to ensure a bacterial concentration of $\sim 10^6$ CFU mL^{-1} . During the experiments, samples were taken at set-times, serial 10-fold dilutions were performed using $\frac{1}{4}$ strength Ringers solutions and six drops of 10 μL were plated on tryptic soy agar (TSA). For samples where low counts were expected, 100 μL -samples with no dilution were plated resulting in a detection limit of 10 CFU mL^{-1} and incubated at 37°C for $> 18 \text{ h}$. After which the average and associated deviation for the number of colonies was calculated.

3. Results and discussion

3.1. Cathode characterisation: Platinum nanoparticles deposited on GDE

The confirmation of Pt nanoparticles deposited on the GDE was performed by using SEM/EDX on all samples as shown in Fig. 3a-d where the red dots are the mapping of Pt by EDX. The EDX spectra showed a strong peak at $\sim 2.04 \text{ keV}$ correlating to the $\text{M}\alpha$ x-ray emission energy of platinum (Fig. S11). The diameter of the nanoparticles (Fig. S12) followed a gamma distribution pattern with a peak diameter at 60–65 nm. Increasing the deposition time increased the total coverage of Pt NP on the electrode, as well as the number of NP greater than 100 nm; the results are comparable those published previously [43].

Table 1

Water parameters of 60 mM Na_2SO_4 compared to stream water before and after autoclaving.

Parameter	60 mM Na_2SO_4	Untreated stream water	Autoclaved stream water
pH	7	8.06	8.36
Dissolved oxygen / mgL^{-1}	8.8	8.5	7.7
Electrical conductivity / mScm^{-1}	10.75	0.675	0.739
Absorption coefficient $\epsilon_{365} / \text{cm}^{-1}$	0.046	0.115	0.117

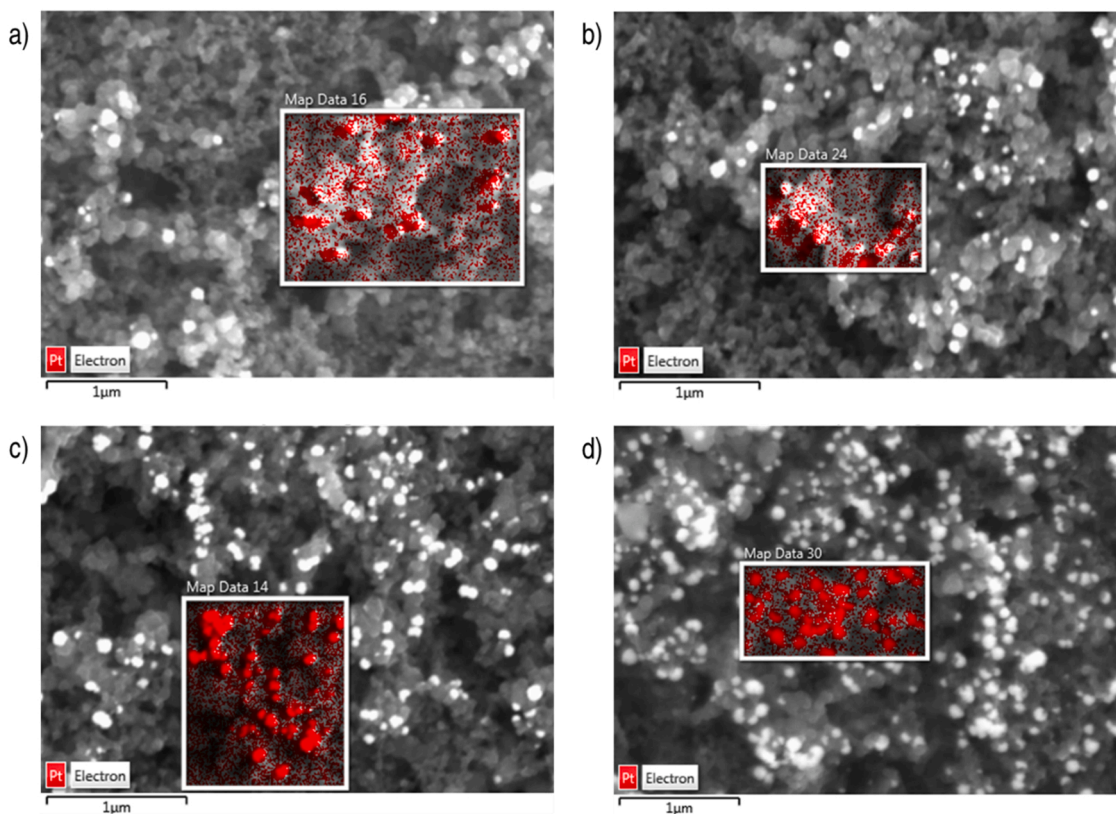


Fig. 3. a-d) EDX maps of Pt nanoparticles (red pixels) for different loadings, a) Pt 10 s, b) Pt 20 s, c) Pt 40 s, d) Pt 80 s.

3.2. Cathode characterisation: oxygen reduction reaction

LSV scans were performed first with nitrogen purging to remove oxygen for a baseline. Air was then purged prior to LSV for oxygen reduction. The results with N₂ and air purging for each material are displayed in Fig. S13 and results in the presence of oxygen (air sparging) are shown in Fig. 4. From the LSV data, the onset potential for the ORR and the current density was determined. The reported definitions for the ORR onset potential vary; these can be either, the point at which current for oxygen reduction is first observed [44], the potential at which -0.1 mA cm^{-2} is reached [45] or by using a line of best fit [46]. Subsequently, there can be 3 different values for the same material and for

the latter method depending on how the line is fitted there can be variations in values obtained. All three methods were examined and the values for each material are stated in Table 2. In all instances the magnitude of the values was in the following order; first observed ORR $< -0.1 \text{ mA cm}^{-2} < \text{line of best fit}$. When comparing the onset potential of two different materials the magnitude is approximately the same for each method; though, the use of -0.1 mA cm^{-2} provides a direct comparison with less error than the other methods.

From the materials examined, carbon felt had the most negative ORR onset potential (-0.458 V (SCE)) at -0.1 mA cm^{-2} , the GDE had a more positive onset potential than the carbon felt, for both the non-hydrophobic side and the hydrophobic side (coated with PTFE). The Pt wire had a more positive onset potential (-0.234 V (SCE)) than the GDE but the Pt modified GDE had the most positive onset potential for oxygen reduction. The addition of platinum NP to GDE (Pt 20 s, 40 s & 80 s) moved the onset potential more positive than the Pt wire, to -0.095 V (SCE) for the highest Pt loading (Pt 80 s). This can be attributed to improved oxygen adsorption on the Pt NP surface which is believed to be a rate-limiting step in the ORR process [47].

In terms of current density, the GDE Pt 40 s performed the best until -1.15 V (SCE) after which Pt had a higher current density, this can be attributed to a change in the reaction from oxygen reduction to water reduction (Eq. 11 [48] N.B. -0.244 V to convert NHE to SCE) as shown in Fig. S14a at potentials greater than -1.0 V (SCE) , Pt shows cathodic current in absence of oxygen, probably hydrogen evolution.

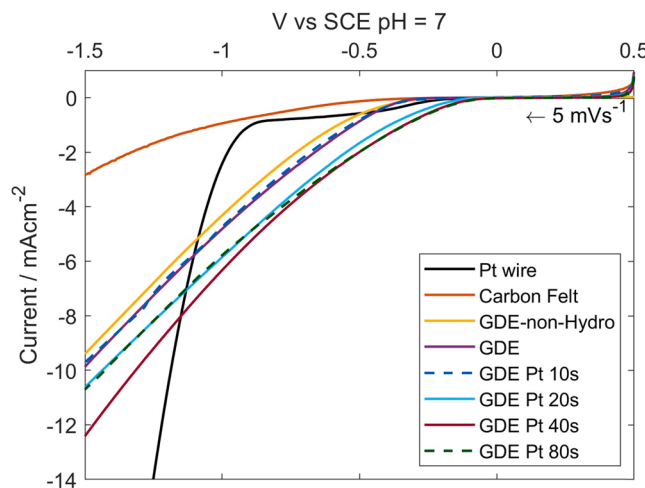


Fig. 4. Compilation of LSV graphs for oxygen reduction, nitrogen plots removed for clarity. Electrolyte 0.1 M KCl, pH 7 and a sweep rate of 5 mV s^{-1} .

Factors influencing choice of cathodic material is to be combined with PEC include; a material with a low onset potential for ORR and current density matching of the counter electrode as to not limit the

Table 2

Onset ORR potential for different materials (V (SCE) pH= 7).

Material	Carbon felt	Pt wire	GDE – non-Hydro	GDE -Hydro	GDE Pt 10 s	GDE Pt 20 s	GDE Pt 40 s	GDE Pt 80 s
First observed ORR	-0.374	-0.174	-0.257	-0.257	-0.257	-0.139	-0.056	-0.047
-0.1 mA cm ⁻²	-0.458	-0.234	-0.378	-0.330	-0.315	-0.145	-0.105	-0.095
Line of best fit	-0.500	-0.250	-0.388	-0.357	-0.351	-0.254	-0.150	-0.194

overall photocurrent.

3.3. Cathode characterisation: ROS (Hydrogen peroxide) generation

Several studies have shown that not only can H₂O₂ inactivate microorganism but there is an associated synergistic effect with UVA irradiation [49–51]. It would therefore be expected that producing H₂O₂ at the counter electrode would enhance the rate of disinfection. The cathode materials were examined for H₂O₂ generation with a fixed potential of – 0.75 V (SCE) as all materials exhibited oxygen reduction at this potential (Fig. 4) in an air saturated solution. The average current density for each material at – 0.75 V is shown in Fig. 5a. The addition of Pt NP increased the current density of the GDE, with Pt 40 s giving the highest current density (–2.46 mA cm⁻²) x1.9 times that of the unmodified GDE. However, the addition of Pt NP at all loadings inhibited the generation of H₂O₂ and this can be attributed to “side-on” adsorption of O₂ on the Pt NP surface which weakens the O–O bond, leading to dissociation of O–O to H₂O and any H₂O₂ generated can be subsequently reduced to H₂O on the Pt cluster (Eq. 7) [52]. To examine if the operating parameters affecting the generation of H₂O₂ when using the Pt GDE, the Pt 80 s sample was further assessed with different potentials and electrolytes, the average current density for each experiment is presented in Fig. S15; however, no H₂O₂ was detected above the detection limit (1 mg L⁻¹) in any of the experiments and no significant drop in the current density was observed.

The unmodified GDE was the only material that showed H₂O₂ generation above the detection limit. When flowing air flow through the non-hydrophobic GDE there was a lower current density when using a higher airflow (14.6 mL s⁻¹) compared to the lower airflow (0.4 mL s⁻¹), due to air bubbles forming on the electrode. The higher airflow also reduced

the Faradaic efficiency. The hydrophobic side had a higher current density and marginally higher Faradaic efficiency (8.4%) than the non-hydrophobic side (Fig. 5b). Operating at a fixed current of 0.2 mA cm⁻² the efficiency increased to 15.5%. The other potential reactions at the cathode are the reduction of H₂O₂ to water (Eq. 7), (Faradic efficiency for H₂O₂ is lower at higher current densities) and/or the direct 4-electron reduction of O₂ to water (Eq. 2) [22]. Compared to literature, the efficiency values obtained in this work are lower, for example, Mudde-mann et al. [53] tested a GDE (Vulcan XC72 carbon black and PTFE on gold-plated nickel wire cloth) at 0.2 mA cm⁻² which displayed a positive linear relationship with pH, though no efficiencies were reported between pH 4–9, if the trend continues in this region an estimated ~50% efficiency would be achieved at pH 7. Their study however used Vulcan XC72 catalyst with a Ag-Ni wire cloth and a cation membrane to prevent oxidation of the H₂O₂ at the anode. In an undivided cell, the concentration of H₂O₂ is also dependent on the material of the anode and size ratio compared to the cathode where the larger cathode is preferred [28]. Barros et al. [29] used unmodified GDE and achieved an efficiency of 33.3% though the experiment was conducted at a higher and more efficient pH (14) and an applied bias of – 1.1 V (Ag/AgCl). Although research has examined the effect of pH on H₂O₂ generation [22,28,53], less research has been preferred on the effect (if any) on the type of supporting electrolyte for the ORR to H₂O₂, although the type of electrolyte has been shown to affect the oxidation of H₂O to yield H₂O₂ (Eq. 7) for metal oxides [54].

The key findings that from the cathode material testing was the non-modified GDE was the only material to produce detectable amounts of H₂O₂ at pH 7 in 0.1 M KCl with the reactor set-up. The GDE with PTFE (hydrophobic side) produced a marginally higher current density & higher Faradaic efficiency. High airflow rate through the GDE not only

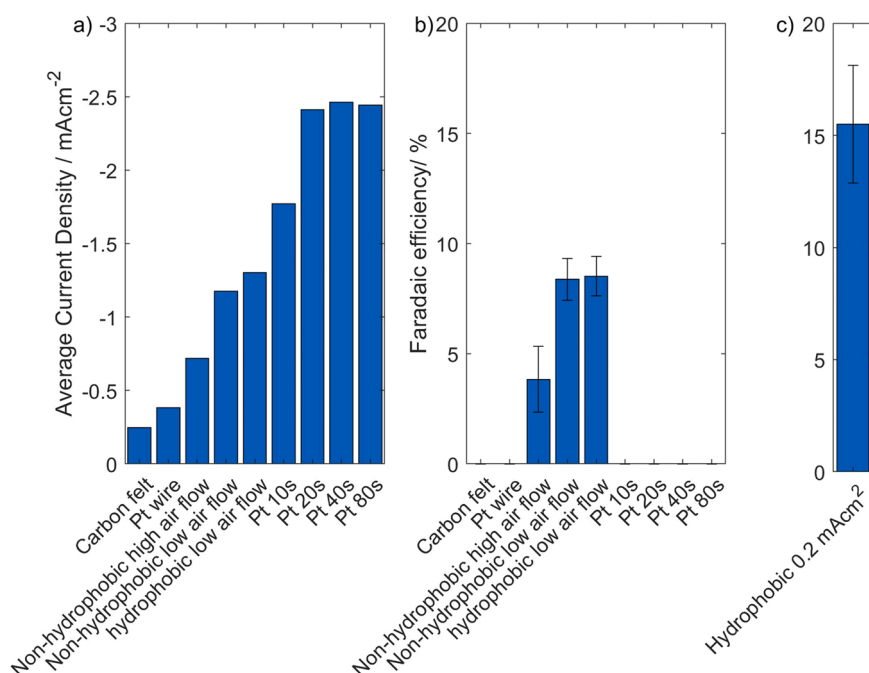


Fig. 5. a) average current density when operating at – 0.75 V (SCE) in 0.1 M KCl, b) the resulting Faradaic efficiency for electrochemical H₂O₂ generation, c) Faradaic efficiency for the hydrophobic GDE when using a fixed current of 0.2 mA cm⁻².

affects the current density but also the efficiency, with low flow rates and low current density being the optimal mode of operation. Whether the generation of H_2O_2 at the cathode improves the rate of inactivation of *E. coli* when combined with PEC is further disused in Section 3.8.

3.4. Photoanode characterisation: nanotube growth

Aligned titania nanotube formation was confirmed via the SEM for all samples. The foil sample is shown in Fig. 6a at 40k magnification and the mesh sample is shown in at 90 magnification and 40k magnification (Fig. 6b-c). The foil NTs had a mean diameter of 102.91 nm with a standard deviation of 15.96 nm, the mesh NTs has a mean diameter of 95.58 nm and a standard deviation of 16.79 nm ($n = 100$). Given the deviation and small sample area for the foil and mesh samples, it is evident that both materials produce comparable nanotubes and similar to those reported in literature for the same conditions [55,56].

3.5. Photoanode characterisation: electrochemical characterisation

The LSV graph for each photoanode is shown in Fig. S16, in all instances, the photocurrent is plateauing at +1.0 V (SCE). The photocurrent vs time response was examined at a fixed potential of +1.0 V (SCE) (Fig. S17) the highest photocurrent was achieved when the TiNT array was annealed at 350 °C as compared to 450 °C for both the foil and mesh samples. Previous reports have suggested 450 °C is optimal annealing temperature for TiO_2 [57,58]. In this work, the highest photocurrent was achieved with the mesh photoanode annealed at 350 °C ($144 \mu\text{A cm}^{-2}$). Although a $1 \times 1 \text{ cm}$ segment of mesh (x3) was irradiated, the true geometric surface area is higher than 1 cm^2 and as such it has been termed normalised photocurrent. The photocurrent is lower than other reports [10] this can be explained due to the preparation route. The concentration of water in the anodising solution has been reported to modify the resultant tubes electrochemical properties. Zhao et al. [59] demonstrated that 2% vol of water in ethylene glycol has a higher photocurrent than 5% vol and at 3% vol (which was used in this study). Water content used in the preparation influence defects at the edge of the tube, however, in literature different sources of irradiation are used (intensity and spectral emission) and different electrolytes are used. The comparison of photoanodes is subsequently difficult; therefore, assessing the IPCE can be a fairer assessment (Fig. 7).

The current at fixed wavelengths is shown in Fig. 7a and the corresponding photon to current conversion efficiency is shown in Fig. 7b. The photoanode is only effective in the UVA range with peak efficiency at 350 nm. The mesh had the highest efficiency of ~60% at 320–350 nm. Comparing to literature, Krbal et al. [60] reported 60% efficiency for a crystalline TiNT array but the peak was 320 nm, the IPCE reduced with lower-energy photons, though the applied potential was lower (+0.4 V (Ag/AgCl)), Gao et al. [61] report ~35% efficiency at 350 nm but also a low potential (+0.5 V (Ag/AgCl)) and Sayantan et al. [62] reported 60% at 350 nm at (+0.4 V (Ag/AgCl)).

The use of artificial irradiance can facilitate the use of a constant and

fixed photonic flux. For real world applications where light intensity varies, it is of interest to examine how the UV intensity correlates to the current density. In these results, a linear correlation is observed (Fig. S18) with intensities less than 100 Wm^{-2} (UV). Therefore, the photocurrent doesn't become saturated by increasing photonic flux in this range and a high photon flux density can be used. This linear correlation has also been reported by Burns et al. [63] when using TiNb_2O_7 photoanode at +1.0 V (RHE) in 0.5 M NaOH (pH 13.4), with a maximum intensity of 2.5 suns (estimated 114 Wm^{-2} of UV).

The IPCE data shows that the most efficient wavelength range for operation is 320–360 nm. If powered by fluorescent UVA lamps their peak output at 365 nm does overlap within this range. The spectrum of a UVA lamp was overlaid on the IPCE results (Fig. S19a), to estimate the efficiency of this irradiation source in generating photocurrent with this photoelectrode. Analysis, using the IPCE and lamp data (Fig. S19b), shows an IPCE of around 30% in the spectral emission range of the lamp. Ideally it is best to match the IPCE to the irradiance source, though it is very common for fluorescent UVA lamps (peak 365 nm) to be with used PEC [4,15,17,20,22,24,64,65] due to cost and availability. The use of an artificial source also enables an anytime method of treatment with a fixed photonic flux enabling a simpler control of the treatment system, although at an additional cost as compared to real sun.

3.6. Photoanode characterisation: ROS (Hydroxyl radical) detection

An increasing fluorescence signal (Fig. S20) indicates the hydroxylation of coumarin to form 7-hydroxycoumarin. The standard curve (Fig. S8) was used to convert the peak intensity to concentration. As the untreated coumarin solution ($T = 0 \text{ min}$) shows a small fluorescence, subsequent measurements were subtracted using the original signal to be able to use the standard curve.

The Faradaic efficiency for $\bullet\text{OH}$ generation for the different photoanodes is shown in Table 3. The highest Faradaic efficiency was achieved with the mesh 350 °C photoanode. When using coumarin as a probe it has been reported that it only detects free $\bullet\text{OH}$ in the bulk solution as the probe doesn't absorb onto the surface of TiO_2 and only 6.1% of the $\bullet\text{OH}$ generated can be detected has 7-hydroxycoumarin [66]. Therefore, the total $\bullet\text{OH}$ can be estimated by dividing the measured 7-hydroxycoumarin by 0.061 (Eq. 12). Though, it has been highlighted that in some instances it is appropriate to apply the same conversion factor to all advanced oxidation processes [67]; thus the original and conversion factor is stated in Table 3.

$$\text{Faradaic efficiency} = \frac{7\text{-hydroxycoumarin molecules}}{\text{No. electrons} \cdot 0.061} \quad (12)$$

A Faradaic efficiency of 1.31% and the generation of 4.43×10^{16} molecules of $\bullet\text{OH}$ was obtained for the mesh 350 °C photoanode. The remaining current may be attributed to oxygen evolution (Eq. 1–2). Nakabayashi et al. [68] reported a high faradaic efficiency (93–105 ± 5%) for oxygen evolution using a rutile single crystal photoanode with (100) facets and a faradaic efficiency of 0.59% for $\bullet\text{OH}$ generation when using coumarin as a probe (0.1 mM) in 0.1 M Na_2SO_4 with a fixed

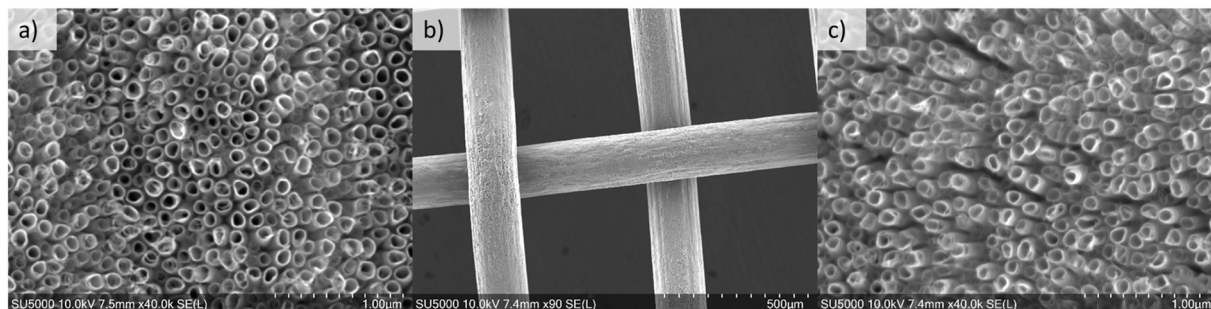


Fig. 6. a) TiNT on foil at 40k magnification, b) TiNT mesh at 90 times magnification, c) TiNT Mesh at 40k magnification.

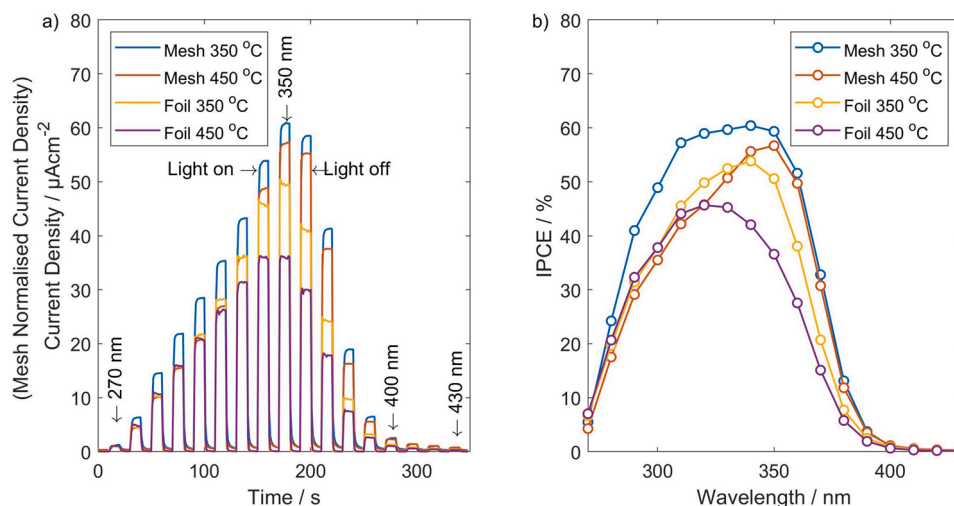


Fig. 7. a) Spectral response for each photoelectrode at different wavelengths from 270 to 430 nm with 10 nm peak-to-peak intervals and 10 s exposure, conducted in 0.1 M KCl at +1.0 V (SCE) and 450 W Xe Lamp, b) the resulting IPCE for each electrode.

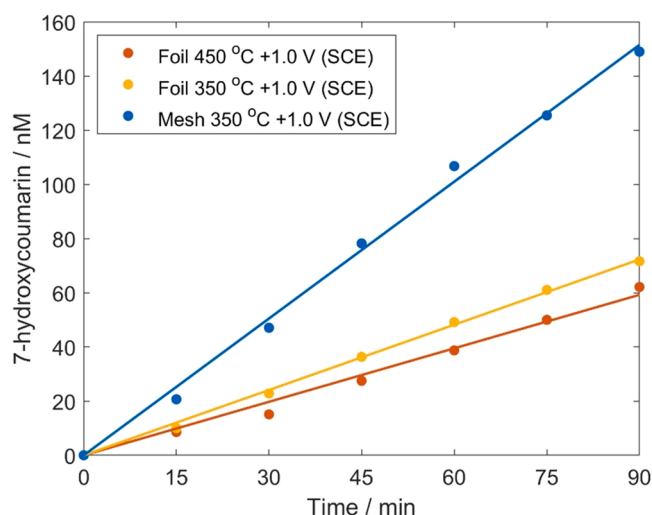


Fig. 8. Generation of 7-hydroxycoumarin for different photoanodes in 0.1 M KCl.

Table 3

Charge, 7-hydroxycoumarin concentration and efficiency for different photoanodes. η_e – Faradaic efficiency; η_{ne} – normalised Faradaic efficiency; η_λ – photonic efficiency in UV range < 400 nm.

Photoanode	Total charge / mC	Concentration of 7-hydroxycoumarin	η_e (%)	η_{ne} (%) / 0.061	η_λ (%)
Mesh 350 °C	522.99	149 nM / 2.7×10^{15} molecules	0.08	1.31	0.013
Foil 350 °C	284.63	71 nM / 1.3×10^{15} molecules	0.07	1.15	0.006
Foil 450 °C	335.67	62 nM / 1.1×10^{15} molecules	0.05	0.82	0.005

potential of +1.3 V (Ag/AgCl) and irradiated with an LED array (365 nm & 70 Wm^{-2}).

3.7. Photoanode characterisation: superoxide detection

The use of the two-compartment cell ensured that only the TiNT electrode was being examined for $\text{O}_2^{\bullet-}$ generation. To confirm that any

decrease in hydroquinone concentration is due to reaction with $\text{O}_2^{\bullet-}$, control experiments were conducted (Fig. 9a). The photolysis control experiment with no scavengers showed a small decrease in the quantity of hydroquinone, which may be attributed to thermal oxidation of hydroquinone to form benzoquinone, autoxidation by molecular oxygen (O_2) is also possible but the reaction rate is pH depended as the deprotonated form of hydroquinone increases (pKa 9.9); as the solution is neutral, autoxidation shouldn't have a noticeable effect on the hydroquinone concentration [69].

To ensure that hydroquinone wasn't oxidised by holes or $\bullet\text{OH}$, KI was used as it's been reported as a hole / $\bullet\text{OH}$ scavenger [39,40] and doesn't interfere with the fluorescence signal when 5 mM was used. The photoanode was tested at +1.0 V (SCE) with the KI scavenger and N_2 to remove oxygen, the reaction rate was slightly less than that of the light control; this demonstrates; firstly, oxidation of hydroquinone is not taking place due to the KI and secondly, any autoxidation of hydroquinone is minimal. When the photoanode was tested with only KI there was a significantly larger decrease in the HQ concentration than with the light control or deoxygenated control. This demonstrates that photo-excited conduction band electrons at the anode can reduce oxygen to $\text{O}_2^{\bullet-}$. This mechanism for oxygen reduction on a photoanode has been suggested by others [10,70] but not experimentally proven until now although oxygen is well known as a photocurrent scavenger for nanoparticulate electrodes.

Additional experiments were conducted using a TiNT electrode foil annealed at 450 °C and a mesh electrode annealed at 350 °C (Fig. 9b). As the generation of $\text{O}_2^{\bullet-}$ is a one-electron reaction and the degradation of 1,4-hydroquinone requires a single $\text{O}_2^{\bullet-}$ the efficiency can be calculated using Eq. 13.

$$\eta_\lambda = \frac{\text{Reduction in 1,4-hydroquinone (molecules)}}{\text{Total number of photons}} \quad (13)$$

The photonic efficiency in the UV range (<400 nm) was then calculated for each electrode (Table 4) under the assumption that one mole of $\text{O}_2^{\bullet-}$ results in the transformation of one mole of hydroquinone. As the light only experiment resulted in a decrease in the HQ concentration, that decrease was considered in the photonic efficiency calculation. These results indicate that more $\text{O}_2^{\bullet-}$ (9.7×10^{17} molecules) was generated compared to $\bullet\text{OH}$ (4.43×10^{16} molecules using convention factor) for the mesh 350 °C photoanode. Comparing the concentration of ROS $\bullet\text{OH}$ and $\text{O}_2^{\bullet-}$ for a TiO_2 photoanode the reductive of O_2 to $\text{O}_2^{\bullet-}$ is an order of magnitude more efficient than for the formation of OH radical.

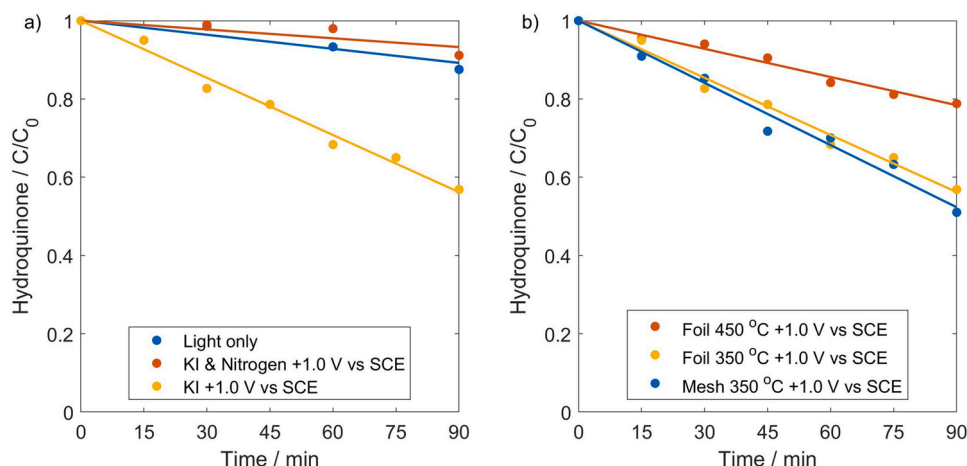


Fig. 9. a) Hydroquinone reduction with a foil TiNT photoanode annealed at 350 °C with control experiments in 0.1 M KCl, b) Hydroquinone concentration vs time for different photoanodes; Foil 450 °C, Foil 350 °C & mesh Foil 450 °C. The applied bias was +1.0 V (SCE) in 0.1 KCl.

Table 4

Reduction in hydroquinone and efficiency for different photoanodes.

Photoanode	Reduction in hydroquinone	η_r (%)
Mesh 350 °C	53.8 μ M / 9.7×10^{17} molecules	4.6
Foil 350 °C	37.0 μ M / 6.7×10^{17} molecules	3.2
Foil 450 °C	4.9 μ M / 1.5×10^{16} molecules	0.42

3.8. Electrode combination (photoanodes and counter electrodes) impact on *E. coli* removal

Two different electrolytes i.e., NaCl and Na₂SO₄ (60 mM) were used in the experiments for the inactivation of *E. coli* using a TiNT photoanode (1.0 × 1.0 cm) annealed at 350 °C with non-modified GDE (2 cm²) with an applied cell bias of +1.0 V (Fig. 10).

When irradiating with only UVA (peak intensity at 365 nm) as a light control, there was no significant reduction in *E. coli* concentration observed (0.06 ± 0.09 log). This can be attributed to the low UVA dose of 22.2 J cm⁻². Song et al. reported a 0.2 log reduction in *E. coli* with 52 J cm⁻² (UVA)[71]. The inactivation of *E. coli* is both dose and wavelength dependent [72]. When testing with the photoanode biased

at +1.0 V there was a major difference in the *E. coli* inactivation rates. For NaCl electrolyte the *E. coli* concentration reached the detection limit after 30 min (5.06 log reduction). In Na₂SO₄ electrolyte the *E. coli* inactivation efficiency was much lower where after 180 min a 2.51 log reduction was observed. The increased rate when using NaCl can be attributed to the generation of reactive chlorine species which are highly effective for the inactivation of *E. coli* [42]. Therefore, to avoid chlorine radicals, Na₂SO₄ can be used to better examine the inactivation of microorganisms attributed to ROS produced by the electrodes.

The I-V curves for different counter electrodes and a Foil TiNT (350 °C) with the UVA lamp are displayed in Fig. S21. The different counter electrodes displayed showed a small deviation from one another at +1.0 V. The non-modified GDE did display marginally higher photocurrent (129 μ A cm⁻²) at +1.0 V though the lowest (Pt 40 s) was 119 μ A cm⁻²; subsequently, the counter electrode wasn't limiting the current significantly due to the low photocurrent produced by the TiNT photoanodes.

The inactivation of *E. coli* when using foil TiNT annealed at 350 °C with the different counter electrodes (Fig. 11a) demonstrates the selection of counter electrode can have a considerable effect on the disinfection rate. The effectiveness of each counter electrode was in the following order GDE > Pt 10 s > Pt 20/40 s > Pt > Pt 80 s. The results show that even a small amount of Pt can negatively impact the rate of disinfection. This can be attributed to the complete reduction of O₂ to H₂O on Pt [11]. It was shown that while that only the non-modified GDE generated H₂O₂ above the detection limit (Fig. 5) and it is known that H₂O₂ in combination with UVA irradiation has a synergetic effect on the inactivation of *E. coli* [26]. There is also the possibility of further reduction of H₂O₂ to \bullet OH (Eq. 14) or generation of O₂^{•-}. Conversely, there is also the potential for cathodic reduction of H₂O₂ to water (Eq. 7) which may be occurring with Pt NT GDE, leading to reduced disinfection rates.

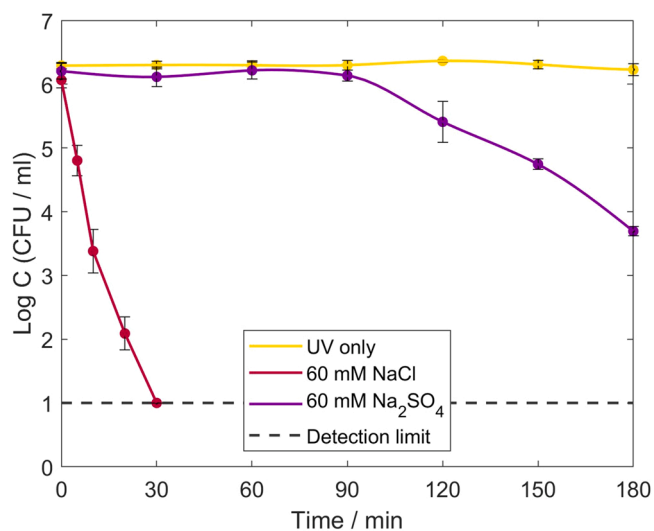


Fig. 10. Inactivation of *E. coli* K12 with a TiNT foil photoanode annealed at 350 °C and operated at +1.0 V cell potential, comparing 60 mM NaCl vs 60 mM Na₂SO₄.

Examination of different photoanodes (Fig. 11b) was conducted with a non-modified GDE as it was the most effective counter electrode. The results display that the foil sample annealed at 350 °C had a higher reduction (2.51 log) compared to the 450 °C (1.39 log); when operated at +1.0 V. This can be attributed to the higher photocurrent, \bullet OH generation (Fig. 8), and higher O₂^{•-} generation for the 350 °C sample (Fig. 9). When the foil sample (350 °C) was tested at higher potentials of +1.5 V & +2.0 V it resulted in reductions of 1.89 & 2.17 log

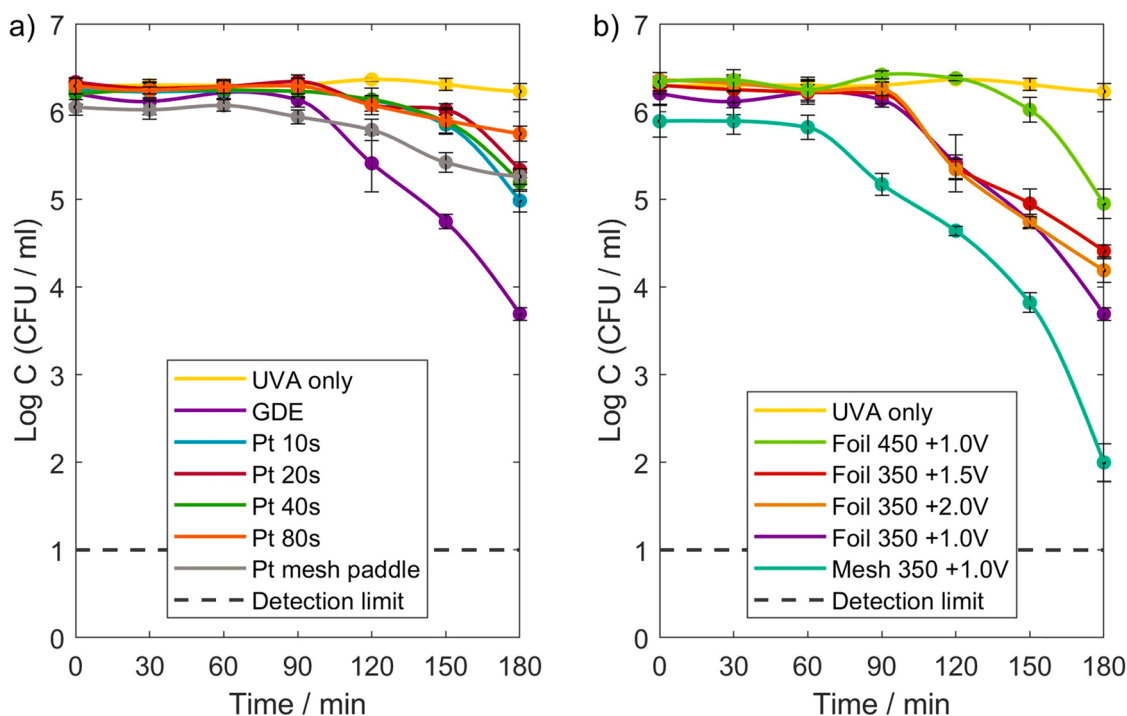


Fig. 11. Inactivation of *E. coli* K12 with a TiNT foil photoanode annealed at 350 °C and operated at + 1.0 V cell potential with different counter electrode materials in 60 mM Na₂SO₄. a) measured CFU.mL⁻¹, b) Inactivation of *E. coli* K12 for different TiNT annealing times, bias and mesh.

respectively, which is lower than what was achieved at + 1.0 V even though there was higher photocurrent. This can be attributed to electro-osmotic repulsion as higher potentials and the high ionic strength solution produces a high ionic concentration gradient at the electrode surface [73]. The mesh photoanode resulted in the highest *E. coli* reduction of 3.89 log, this can be attributed to the larger geometric surface area, higher photocurrent, •OH generation (Fig. 8) and O₂^{•-} generated (Fig. 9). None of the photoanodes reached the detection limit in the 3 h of the experiments due to the low surface to volume ratio (0.067 cm² cm⁻³) characterised by a long lag time before any *E. coli* inactivation was observed.

3.9. Scaling up: inactivation using a thin cell reactor

As the mesh photoanode showed a high disinfection efficiency it enables the construction of a thin one-compartment cell reactor, to increase the surface area to volume ratio to 2.01 cm² cm⁻³, 30 times higher than the previous set-up. This results in a considerable change in the disinfection rate (Fig. 12), as previously the detection limit wasn't reached, but with the thin cell, the detection limit was reached in 90 min (5.17 log reduction,) under the same conditions but with marginally less UV intensity. High surface-to-volume ratios have been shown to improved reaction efficiencies Wang et al. [74] for the degradation of methylene blue and Bai et al. [3] for the degradation of tetracycline. The lag time has also been reduced from 60 min to 5 min, therefore PEC reactors with a long lag time may be an indication of a defect in one of the design or operational parameters.

Increasing the UV intensity in our thin cell reactor to 45.6 Wm⁻² resulted in an even faster *E. coli* inactivation rate and no observed lag period, reaching the detection limit in 20 min. Due to a lower initial concentration complete inactivation was a 4.56 log reduction. To further test the reactor, a natural water source (local stream water) was used, with no added electrolytes and autoclaved before use to inactivate any naturally present microorganisms. The photocurrent response for the thin cell reactor with Na₂SO₄ and with stream water is shown in Fig. S22. Although the conductivity of the two solutions are markedly

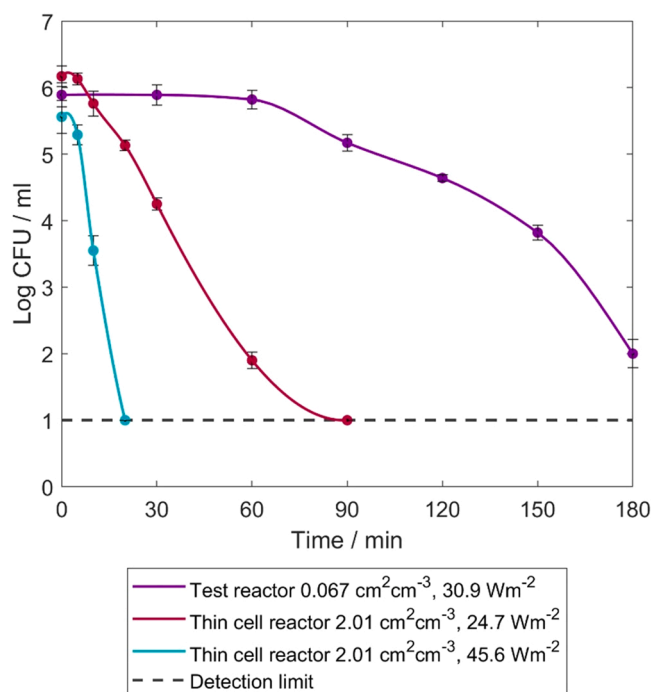


Fig. 12. The effect of different surface to volume ratio and UV intensity for the inactivation of *E. coli* K12 in 60 mM of Na₂SO₄ using mesh TiNT electrode annealed at 350 °C with a non-modified GDE with + 1.0 V cell bias.

different, 10.75 mS cm⁻¹ (Na₂SO₄) & 0.739 mS cm⁻¹ (stream water), and stream water has a higher absorption coefficient at 365 nm, there is only a 25% reduction in the observed photocurrent (4.8 mA – stream water). This is due to the small distance separating the electrodes, limiting the IR drop; subsequently the conductivity of the solution is of less importance in a thin cell reactor. The most distinguishable

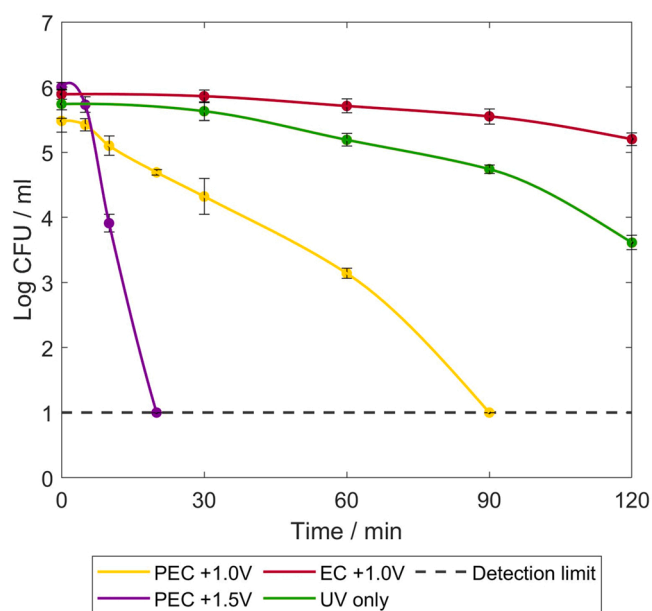


Fig. 13. Inactivation of *E. coli* K12 in stream water using a thin cell reactor.

difference between the two electrolytes is the point of photocurrent saturation with Na_2SO_4 the photocurrent starts to saturate at +1.0 V while with the stream water the saturation begins at around +1.5 V due to the difference in electrolyte conductivity. With only UVA there was a larger reduction in the *E. coli* (2.13 log) show in Fig. 13 compared to previous experiments (0.06 log). This can be attributed to the higher UV intensity, smaller optical pathlength of the solution and the presence of dissolved organic matter (DOM); as Zhang et al. [75] demonstrated, the presence of $10\text{--}50\text{ mg L}^{-1}$ (DOM), there was an increase in the photodegradation of free nucleic acids base pairs by a factor of 1.85–14.6 times compared to without DOM.

When applying +1.0 V it takes 90 min to reach the detection limit while with Na_2SO_4 the time was only 20 min. The increased time to reach the detection limit with the stream water can be explained by the 25% reduction in the photocurrent (4.8 mA) and because of the presence of DOM; although beneficial in UV inactivation, when applied with PEC the DOM can absorb UV photons and compete for h^+ and $\bullet\text{OH}$ [76,77]. As shown in Fig. S22 the photocurrent continues to rise linearly with the stream water up to +1.5 V. At +1.5 V it took 20 min to reach the detection limit (5.0 log). At the higher potential (+1.5 V), the photocurrent increased to 6.7 mA higher than Na_2SO_4 at +1.0 V (6.0 mA). The higher bias and low ionic strength of the stream water improves the electrophoretic mobility [78] and because of the low ionic strength the effect of electrostatic repulsion at the electrode is reduced [73]. The higher photocurrent at +1.5 V and the small gap between the electrodes, overcome the adverse effects of the low conductivity and DOM, reporting similar results when using 60 mM Na_2SO_4 at +1.0 V. The results obtained in this study have been compared to several other reactors for inactivation of *E. coli* K12 from literature, compiled into Table S4. It would appear that the thin cell reactor in this work is an improvement on existing designs; however, direct comparison of reactors from literature can be difficult due to the number of variables involved, e.g. volume treated, electrodes used, electrolyte solution and irradiation profile.

4. Conclusions

For cathode materials, the use of Pt NT on GDE results in a lower onset potential for ORR compared to the Pt wire. However, the inclusion of Pt on the GDE inhibits the generation of H_2O_2 to below the detection

limit. When using the GDE there was marginally higher current and Faradaic efficiency with the PTFE coated side, a high airflow rate through the electrode can impact on current and the Faradaic efficiency, and a lower current density results in higher Faradaic efficiency. When examining the counter electrodes for the inactivation of *E. coli* the non-modified GDE has the highest disinfection rate and with increasing Pt NP loadings a lower rate of inactivation was observed; subsequently, we can extract from the results that the generation of H_2O_2 at the counter electrode is beneficial with PEC for disinfection.

The use of artificial irradiance can enable on-demand water treatment, with a fixed flux and as photocurrent scales linear response with UV intensity (till at least 100 W m^{-2}) high intensities can be used without saturating the photocurrent. There is also an opportunity to explore the use of solar concentrating systems. The TiNT electrode was experimentally proven to produce superoxide radical. The generation of reductive reaction at the photoanode suggests that photocurrent alone is an inappropriate method to measure activity and the measurement of ROS concentration a potentially better measure of the activity of a system.

A reactor with a high surface to volume ratio is required to increase the rate of the inactivation of microorganisms and overcome the adverse effects of low conductivity and the presence of DOM. The thin cell reactor using materials optimised for ROS production (a non-modified GDE and a combined TiNT mesh photoanode) with an applied bias of +1.5 V was tested using stream water resulted in a 5.0 log reduction of *E. coli*, reaching the detection limit in 20 min with 45.6 W m^{-2} (5.4 J cm^{-2}). Further development of the reactor is required, such as introducing a flow system, increasing the irradiance intensity, assessing improvements to the photoanode and counter electrode to improve the selectivity of the ORR to yield ROS.

CRediT authorship contribution statement

S. McMichael: Conceptualisation, Methodology, Investigation, Writing - Original Draft, Writing - review & editing. **A. Tolosana-Moranchel:** Methodology and Writing - review & editing. **M.A.L.R.M. Cortes:** Investigation and Writing - review & editing. **J.W.J. Hamilton:** Methodology, Writing - review & editing. **P. Fernandez-Ibanez:** Funding acquisition, Supervision, Writing - review & editing. **J.A. Byrne:** Funding acquisition, Supervision, Writing - review & editing.

Declaration of Competing Interest

The authors declare that they have no known competing financial interests or personal relationships that could have appeared to influence the work reported in this paper.

Acknowledgements

The authors wish to acknowledge the Department for Economy (DfE) Northern Ireland for funding Stuart McMichael, the Global Challenges Research Fund (GCRF) UK Research and Innovation for funding SAFE-WATER (Grant Reference EP/P032427/1) and European Union's Horizon 2020 research and innovation programme under grant agreement No 820718 (PANIWATER).

Appendix A. Supporting information

Supplementary data associated with this article can be found in the online version at [doi:10.1016/j.apcatb.2022.121339](https://doi.org/10.1016/j.apcatb.2022.121339).

References

- [1] S. McMichael, P. Fernández-Ibáñez, J.A. Byrne, A review of photoelectrocatalytic reactors for water and wastewater treatment, *Water* 13 (2021) 1198, <https://doi.org/10.3390/w13091198>.

- [2] J.Y.U. Kim, G.G. Bessegeto, B.C. de Souza, J.J. da Silva, M.V.B. Zanoni, Efficient treatment of swimming pool water by photoelectrocatalytic ozonation: inactivation of *Candida parapsilosis* and mineralization of Benzophenone-3 and urea, *Chem. Eng. J.* 378 (2019), 122094, <https://doi.org/10.1016/j.cej.2019.122094>.
- [3] J. Bai, Y. Liu, J. Li, B. Zhou, Q. Zheng, W. Cai, A novel thin-layer photoelectrocatalytic (PEC) reactor with double-faced titania nanotube arrays electrode for effective degradation of tetracycline, *Appl. Catal. B* 98 (2010) 154–160, <https://doi.org/10.1016/j.apcatb.2010.05.024>.
- [4] I. Salmerón, P.K. Sharma, M.I. Polo-López, A. Tolosana, S. McMichael, I. Oller, J. A. Byrne, P. Fernández-Ibáñez, Electrochemically assisted photocatalysis for the simultaneous degradation of organic micro-contaminants and inactivation of microorganisms in water, *Process Saf. Environ. Prot.* 147 (2021) 488–496, <https://doi.org/10.1016/j.psep.2020.09.060>.
- [5] W.A. Abbas, I.H. Abdullah, B.A. Ali, N. Ahmed, A.M. Mohamed, M.Y. Rezk, N. Ismail, M.A. Mohamed, N.K. Allam, Recent advances in the use of TiO₂ nanotube powder in biological, environmental, and energy applications, *Nanoscale Adv.* 1 (2019) 2801–2816, <https://doi.org/10.1039/C9NA00339H>.
- [6] Y. Feng, H.H.M. Rijnaarts, D. Yntema, Z. Gong, D.D. Dionysiou, Z. Cao, S. Miao, Y. Chen, Y. Ye, Y. Wang, Applications of anodized TiO₂ nanotube arrays on the removal of aqueous contaminants of emerging concern: a review, *Water Res.* 186 (2020), 116327, <https://doi.org/10.1016/j.watres.2020.116327>.
- [7] S. McMichael, M. Waso, B. Reyneke, W. Khan, J.A. Byrne, P. Fernandez-Ibanez, Electrochemically assisted photocatalysis for the disinfection of rainwater under solar irradiation, *Appl. Catal. B* 281 (2021), 119485, <https://doi.org/10.1016/j.apcatb.2020.119485>.
- [8] B. Gao, M. Sun, W. Ding, Z. Ding, W. Liu, Decoration of γ -graphyne on TiO₂ nanotube arrays: Improved photoelectrochemical and photoelectrocatalytic properties, *Appl. Catal. B* 281 (2021), 119492, <https://doi.org/10.1016/j.apcatb.2020.119492>.
- [9] X. Wang, M. Sun, M. Murugananthan, Y. Zhang, L. Zhang, Electrochemically self-doped WO₃/TiO₂ nanotubes for photocatalytic degradation of volatile organic compounds, *Appl. Catal. B* 260 (2020), 118205, <https://doi.org/10.1016/j.apcatb.2019.118205>.
- [10] C. Pablos, J. Marugán, R. van Grieken, P.S.M. Dunlop, J.W.J. Hamilton, D. D. Dionysiou, J.A. Byrne, Electrochemical enhancement of photocatalytic disinfection on aligned TiO₂ and nitrogen doped TiO₂ nanotubes, *Molecules* 22 (2017) 704, <https://doi.org/10.3390/molecules22050704>.
- [11] M. Zhou, H. Wang, S. Guo, Towards high-efficiency nanoelectrocatalysts for oxygen reduction through engineering advanced carbon nanomaterials, *Chem. Soc. Rev.* 45 (2016), <https://doi.org/10.1039/c5cs00414d>, 1273–137.
- [12] B. Gao, J. An, Y. Wang, J. Liu, L. Wang, M. Sillanpää, Functional photoelectrocatalytic membrane fabricated from ZnIn₂S₄, PVDF and carbon fibre for continuous removal of tetracycline, *J. Solid State Chem.* 290 (2020), 121525, <https://doi.org/10.1016/j.jssc.2020.121525>.
- [13] X. Wang, G. Wang, S. Chen, X. Fan, X. Guan, H. Yu, Integration of membrane filtration and photoelectrocatalysis on g-C₃N₄/CNTs/Al₂O₃ membrane with visible-light response for enhanced water treatment, *J. Membr. Sci.* 541 (2017) 153–161, <https://doi.org/10.1016/j.memsci.2017.06.046>.
- [14] Andreia Betina Kreuser dos Santos, E.M.T. Claro, R.N. Montagnolli, J.M. Cruz, P.R. M. Lopes, E.D. Bidoia, Electrochemically assisted photocatalysis: highly efficient treatment using thermal titanium oxides doped and non-doped electrodes for water disinfection, *Environ. Manag. Today* 204 (2017) 255–263, <https://doi.org/10.1016/j.jenvman.2017.09.006>.
- [15] C. Pablos, J. Marugán, C. Adán, M. Osuna, R. van Grieken, Performance of TiO₂ photoanodes toward oxidation of methanol and *E. coli* inactivation in water in a scaled-up photoelectrocatalytic reactor, *Electrochim. Acta* 258 (2017) 599–606, <https://doi.org/10.1016/j.electacta.2017.11.103>.
- [16] P.A. Christensen, T.P. Curtis, T.A. Egerton, S.A.M. Kosa, J.R. Tinlin, Photoelectrocatalytic and photocatalytic disinfection of *E. coli* suspensions by titanium dioxide, *Appl. Catal. B* 41 (2003) 371–386, [https://doi.org/10.1016/S0926-3373\(02\)00172-8](https://doi.org/10.1016/S0926-3373(02)00172-8).
- [17] T.A. McMurray, J.A. Byrne, P.S.M. Dunlop, E.T. McAdams, Photocatalytic and electrochemically assisted photocatalytic oxidation of formic acid on TiO₂ films under UVA and UVB irradiation, *J. Appl. Electrochem.* 35 (2005) 723–731, <https://doi.org/10.1007/s10800-005-1397-1>.
- [18] P.S. Shinde, P.S. Patil, P.N. Bhosale, A. Brüger, G. Nauer, M. Neumann-Spallart, C. H. Bhosale, UVA and solar light assisted photoelectrocatalytic degradation of AO7 dye in water using spray deposited TiO₂ thin films, *Appl. Catal. B* 89 (2009) 288–294, <https://doi.org/10.1016/j.apcatb.2009.02.025>.
- [19] X. Mei, J. Bai, S. Chen, M. Zhou, P. Jiang, C. Zhou, F. Fang, Y. Zhang, J. Li, M. Long, B. Zhou, Efficient SO₂ removal and highly synergistic H₂O₂ production based on a novel dual-function photoelectrocatalytic system, *Environ. Sci. Technol.* 54 (2020) 11515–11525, <https://doi.org/10.1021/acs.est.0c00886>.
- [20] E. Mousset, V. Huang Weiqi, B. Foong Yang Kai, J.S. Koh, J.W. Tng, Z. Wang, O. Lefebvre, A new 3D-printed photoelectrocatalytic reactor combining the benefits of a transparent electrode and the Fenton reaction for advanced wastewater treatment, *J. Mater. Chem. A* 5 (2017) 24951–24964, <https://doi.org/10.1039/c7ta08182k>.
- [21] P. Fernandez-Ibáñez, S. Malato, O. Enea, Photoelectrochemical reactors for the solar decontamination of water, *Catal. Today* 54 (1999) 329–339, [https://doi.org/10.1016/S0920-5861\(99\)00194-7](https://doi.org/10.1016/S0920-5861(99)00194-7).
- [22] W.H. Leng, W.C. Zhu, J. Ni, Z. Zhang, J.Q. Zhang, C.N. Cao, Photoelectrocatalytic destruction of organics using TiO₂ as photoanode with simultaneous production of H₂O₂ at the cathode, *Appl. Catal. A-Gen.* 300 (2006) 24–35, <https://doi.org/10.1016/j.apcata.2005.10.053>.
- [23] A.S. Martins, A. Lachgar, M.V. Boldrin Zanoni, Sandwich Nylon/stainless-steel/WO₃ membrane for the photoelectrocatalytic removal of Reactive Red 120 dye applied in a flow reactor, *Sep. Purif. Technol.* 237 (2020), 116338, <https://doi.org/10.1016/j.seppur.2019.116338>.
- [24] X. Liu, Y. Han, G. Li, H. Zhang, H. Zhao, Instant inactivation and rapid decomposition of *Escherichia coli* using a high efficiency TiO₂ nanotube array photoelectrode, *RSC Adv.* 3 (2013) 20824–20828, <https://doi.org/10.1039/C3RA43708f>.
- [25] S. Adhikari, S. Selvaraj, D. Kim, Construction of heterojunction photoelectrode via atomic layer deposition of Fe₂O₃ on Bi₂WO₆ for highly efficient photoelectrochemical sensing and degradation of tetracycline, *Appl. Catal. B* 244 (2019) 11–24, <https://doi.org/10.1016/j.apcatb.2018.11.043>.
- [26] L. Feng, C. Peillex-Delphe, C. Lü, D. Wang, S. Giannakis, C. Pulgarin, Employing bacterial mutations for the elucidation of photo-Fenton disinfection: focus on the intracellular and extracellular inactivation mechanisms induced by UVA and H₂O₂, *Water Res.* 182 (2020), 116049, <https://doi.org/10.1016/j.watres.2020.116049>.
- [27] G. Ferro, M.I. Polo-López, A.B. Martínez-Piernas, P. Fernández-Ibáñez, A. Agüera, L. Rizzo, Cross-contamination of residual emerging contaminants and antibiotic resistant bacteria in lettuce crops and soil irrigated with wastewater treated by sunlight/H₂O₂, *Environ. Sci. Technol.* 49 (2015) 11096–11104, <https://doi.org/10.1021/acs.est.5b02613>.
- [28] P. Ma, H. Ma, A. Galia, S. Sabatino, O. Scialdone, Reduction of oxygen to H₂O₂ at carbon felt cathode in undivided cells. Effect of the ratio between the anode and the cathode surfaces and of other operative parameters, *Sep. Purif. Technol.* 208 (2019) 116–122, <https://doi.org/10.1016/j.seppur.2018.04.062>.
- [29] W.R.P. Barros, T. Ereno, A.C. Tavares, M.R.V. Lanza, In situ electrochemical generation of hydrogen peroxide in alkaline aqueous solution by using an unmodified gas diffusion electrode, *ChemElectroChem* 2 (2015) 714–719, <https://doi.org/10.1002/celec.201402426>.
- [30] Q. Zhang, M. Zhou, G. Ren, Y. Li, Y. Li, X. Du, Highly efficient electrosynthesis of hydrogen peroxide on a superhydrophobic three-phase interface by natural air diffusion, *Nat. Commun.* 11 (2020) 1731, <https://doi.org/10.1038/s41467-020-15597-y>.
- [31] V.C. Bleich, N.G. Andrew, M.J. Martin, G.P. Mulcahy, A.M. Pauli, S.S. Rosenstock, Quality of Water Available to Wildlife in Desert Environments: Comparisons Among Anthropogenic and Natural Sources, *Wildl. Soc. Bull.* 34, 627–632. [https://doi.org/10.2193/0091-7648\(2006\)34\[627:QOWATW\]2.0.CO;2](https://doi.org/10.2193/0091-7648(2006)34[627:QOWATW]2.0.CO;2).
- [32] M.M.E. Duarte, A.S. Pilla, J.M. Sieben, C.E. Mayer, Platinum particles electrodeposition on carbon substrates, *Electrochem. Commun.* 8 (2006) 159–164, <https://doi.org/10.1016/j.elecom.2005.11.003>.
- [33] C.A. Schneider, W.S. Rasband, K.W. Eliceiri, NIH Image to ImageJ: 25 years of image analysis, *Nat. Methods* 9 (2012) 671–675, <https://doi.org/10.1038/Nmeth.2089>.
- [34] G.M. Eisenberg, Colorimetric determination of hydrogen peroxide, *Ind. Eng. Chem. Anal. Ed.* 15 (1943) 327–328, <https://doi.org/10.1021/i560117a011>.
- [35] S. Yeonmi, L. Seonghoon, Self-organized regular arrays of anodic TiO₂ nanotubes, *Nano Lett.* 8 (2008) 3171–3173, <https://doi.org/10.1021/nl801422w>.
- [36] V. Leandri, J.M. Gardner, M. Jonsson, Coumarin as a quantitative probe for hydroxyl radical formation in heterogeneous photocatalysis, *J. Phys. Chem. C* 123 (2019) 6667–6674, <https://doi.org/10.1021/acs.jpcc.9b00337>.
- [37] Y. Nosaka, A.Y. Nosaka, Comment on “Coumarin as a quantitative probe for hydroxyl radical formation in heterogeneous photocatalysis”, *J. Phys. Chem. C* 123 (2019) 20682–20684, <https://doi.org/10.1021/acs.jpcc.9b04190>.
- [38] O. Fónagy, E. Szabó-Bárdos, O. Horváth, 1,4-Benzoquinone and 1,4-hydroquinone based determination of electron and superoxide radical formed in heterogeneous photocatalytic systems, *J. Photochem. Photobiol. A* 407 (2021), 113057, <https://doi.org/10.1016/j.jphotochem.2021.113057>.
- [39] W. Raza, S.M. Faisal, M. Owais, D. Bahnemann, M. Muneer, Facile fabrication of highly efficient modified ZnO photocatalyst with enhanced photocatalytic, antibacterial and anticancer activity, *RSC Adv.* 6 (2016) 78335–78350, <https://doi.org/10.1039/C6RA06774C>.
- [40] J.T. Schneider, D.S. Firak, R.R. Ribeiro, P. Peralta-Zamora, Use of scavenger agents in heterogeneous photocatalysis: truths, half-truths, and misinterpretations, *Phys. Chem. Chem. Phys.* 22 (2020) 15723–15733, <https://doi.org/10.1039/D0CP02411B>.
- [41] M. Zhu, J. Lu, Y. Hu, Y. Liu, S. Hu, C. Zhu, Photochemical reactions between 1,4-benzoquinone and O₂, *Environ. Sci. Pollut. Res.* 27 (2020) 31289–31299, <https://doi.org/10.1007/s11356-020-09422-8>.
- [42] M.S. Koo, X. Chen, K. Cho, T. An, W. Choi, In situ photoelectrochemical chloride activation using a WO₃ electrode for oxidative treatment with simultaneous H₂ evolution under visible light, *Environ. Sci. Technol.* 53 (2019) 9926–9936, <https://doi.org/10.1021/acs.est.9b02401>.
- [43] J. Feng, A. Li, A. Wang, Z. Lei, J. Chen, Electrodeposition of monodispersed platinum nanoparticles on a glassy carbon electrode for sensing methanol, *Microchim. Acta* 173 (2011) 383–389, <https://doi.org/10.1007/s00604-011-0566-7>.
- [44] R. Wang, K. Wang, Z. Wang, H. Song, H. Wang, S. Ji, Pig bones derived N-doped carbon with multi-level pores as electrocatalyst for oxygen reduction, *J. Power Sources* 297 (2015) 295–301, <https://doi.org/10.1016/j.jpowsour.2015.07.107>.
- [45] H. Zhao, C. Sun, Z. Jin, D. Wang, X. Yan, Z. Chen, G. Zhu, X. Yao, Carbon for the oxygen reduction reaction: a defect mechanism, *J. Mater. Chem. A* 3 (2015) 11736–11739, <https://doi.org/10.1039/C5TA02229K>.
- [46] T. Tran, M.Y. Song, K.P. Singh, D. Yang, J. Yu, Iron–polypyrrole electrocatalyst with remarkable activity and stability for ORR in both alkaline and acidic conditions: a comprehensive assessment of catalyst preparation sequence, *J. Mater. Chem. A* 4 (2016) 8645–8657, <https://doi.org/10.1039/C6TA01543C>.

- [47] X. Huang, T. Shen, T. Zhang, H. Qiu, X. Gu, Z. Ali, Y. Hou, Efficient oxygen reduction catalysts of porous carbon nanostructures decorated with transition metal species, *Adv. Energy Mater.* 10 (2020), 1900375, <https://doi.org/10.1002/aenm.201900375>.
- [48] W.M. Haynes, D.R. Lide, T.J. Bruno, *CRC Handbook of Chemistry and Physics*, 97th edition, CRC Press, Boca Raton, Florida, 2016.
- [49] T.W. Ng, T. An, G. Li, W.K. Ho, H.Y. Yip, H. Zhao, P.K. Wong, The role and synergistic effect of the light irradiation and H₂O₂ in photocatalytic inactivation of *Escherichia coli*, *J. Photochem. Photobiol. B* 149 (2015) 164–171, <https://doi.org/10.1016/j.jphotobiol.2015.06.007>.
- [50] I. García-Fernández, S. Miralles-Cuevas, I. Oller, S. Malato, P. Fernández-Ibáñez, M. I. Polo-López, Inactivation of *E. coli* and *E. faecalis* by solar photo-Fenton with EDDS complex at neutral pH in municipal wastewater effluents, *J. Hazard. Mater.* 372 (2019) 85–93, <https://doi.org/10.1016/j.jhazmat.2018.07.037>.
- [51] P. Sun, C. Tyree, C. Huang, Inactivation of *Escherichia coli*, Bacteriophage MS2, and *Bacillus Spores* under UV/H₂O₂ and UV/peroxydisulfate advanced disinfection conditions, *Environ. Sci. Technol.* 50 (2016) 4448–4458, <https://doi.org/10.1021/acs.est.5b06097>.
- [52] C.H. Choi, H.C. Kwon, S. Yook, H. Shin, H. Kim, M. Choi, Hydrogen peroxide synthesis via enhanced two-electron oxygen reduction pathway on carbon-coated Pt surface, *J. Phys. Chem. C* 118 (2014) 30063–30070, <https://doi.org/10.1021/jp5113894>.
- [53] T. Muddemann, D.R. Haupt, M. Sievers, U. Kunz, Improved operating parameters for hydrogen peroxide-generating gas diffusion electrodes, *Chem. Ing. Tech.* 92 (2020) 505–512, <https://doi.org/10.1002/cite.201900137>.
- [54] K. Fukui, Y. Miyase, Y. Mieseki, T. Gunji, K. Sayama, Enhanced oxidative hydrogen peroxide production on conducting glass anodes modified with metal oxides, *ChemistrySelect* 1 (2016) 5721–5726, <https://doi.org/10.1002/slct.201601469>.
- [55] S. Li, S. Lin, J. Liao, N. Pan, D. Li, J. Li, Nitrogen-doped TiO₂ nanotube arrays with enhanced photoelectrochemical property, *Int. J. Photoenergy* 2012 (2012), 794207, <https://doi.org/10.1155/2012/794207>.
- [56] M.A.L.R.M. Cortes, S. McMichael, J.W.J. Hamilton, P.K. Sharma, A. Brown, J. A. Byrne, Photoelectrochemical reduction of CO₂ with TiNT, *Mater. Sci. Semicond. Process.* 108 (2020), 104900, <https://doi.org/10.1016/j.mssp.2019.104900>.
- [57] Z. Xie, S. Shuang, L. Ma, F. Zhu, X. Liu, Z. Zhang, Annealing effect on the photoelectrochemical and photocatalytic performance of TiO₂ nanorod arrays, *RSC Adv.* 7 (2017) 51382–51390, <https://doi.org/10.1039/c7ra09801d>.
- [58] S. Ali, H. Granbohm, J. Lahtinen, S. Hannula, Titania nanotubes prepared by rapid breakdown anodization for photocatalytic decolorization of organic dyes under UV and natural solar light, *Nanoscale Res. Lett.* 13 (2018) 1–14, <https://doi.org/10.1186/s11671-018-2591-5>.
- [59] Y. Sun, Q. Zhao, G. Wang, K. Yan, Influence of water content on the formation of TiO₂ nanotubes and photoelectrochemical hydrogen generation, *J. Alloy. Compd.* 711 (2017) 514–520, <https://doi.org/10.1016/j.jallcom.2017.03.007>.
- [60] M. Krbal, J. Kucharik, H. Sopha, H. Nemec, J.M. Macak, Charge transport in anodic TiO₂ nanotubes studied by terahertz spectroscopy, *Phys. Status Solidi A* 10 (2016) 691–695, <https://doi.org/10.1002/pssr.201600179>.
- [61] Z. Gao, Y. Qu, X. Zhou, L. Wang, Y. Song, P. Schmuki, Pt-decorated g-C₃N₄/TiO₂ nanotube arrays with enhanced visible-light photocatalytic activity for H₂ evolution, *ChemistryOpen* 5 (2016) 197–200, <https://doi.org/10.1002/open.201500219>.
- [62] S. Das, H. Sopha, M. Krbal, R. Zazpe, V. Podzemna, J. Prikrýl, J.M. Macak, Electrochemical infilling of CuInSe₂ within TiO₂ nanotube layers and subsequent photoelectrochemical studies, *ChemElectroChem* 4 (2017) 495–499, <https://doi.org/10.1002/celec.201600763>.
- [63] E.W. Burns, D. Pergolesi, T.J. Schmidt, T. Lippert, V. Daramalla, Systematic material study reveals TiNb₂O₇ as a model wide-bandgap photoanode material for solar water splitting, *Chem. Eur. J.* 26 (2020) 7065–7073, <https://doi.org/10.1002/chem.201905444>.
- [64] W.H. Leng, Z. Zhang, J.Q. Zhang, Photoelectrocatalytic degradation of aniline over rutile TiO₂/Ti electrode thermally formed at 600 °C, *J. Mol. Catal. A Chem.* 206 (2003) 239–252, [https://doi.org/10.1016/S1381-1169\(03\)00373-X](https://doi.org/10.1016/S1381-1169(03)00373-X).
- [65] N. Nordin, L. Ho, S. Ong, A.H. Ibrahim, S. Lee, Y. Ong, Elucidating the effects of different photoanode materials on electricity generation and dye degradation in a sustainable hybrid system of photocatalytic fuel cell and peroxi-coagulation process, *Chemosphere* 214 (2019) 614–622, <https://doi.org/10.1016/j.chemosphere.2018.09.144>.
- [66] J. Zhang, Y. Nosaka, Mechanism of the OH radical generation in photocatalysis with TiO₂ of different crystalline types, *J. Phys. Chem. C* 118 (2014) 10824–10832, <https://doi.org/10.1021/jp501214m>.
- [67] S.J. De-Nasri, S. Nagarajan, P.K.J. Robertson, V.V. Ranade, Quantification of hydroxyl radicals in photocatalysis and acoustic cavitation: Utility of coumarin as a chemical probe, *Chem. Eng. J.* (2020), 127560, <https://doi.org/10.1016/j.cej.2020.127560>.
- [68] Y. Nakabayashi, Y. Nosaka, OH radical formation at distinct faces of rutile TiO₂ crystal in the procedure of photoelectrochemical water oxidation, *J. Phys. Chem. C* 117 (2013) 23832–23839, <https://doi.org/10.1021/jp408244h>.
- [69] Y. Song, G.R. Buettner, Thermodynamic and kinetic considerations for the reaction of semiquinone radicals to form superoxide and hydrogen peroxide, *Free Radic. Biol. Med.* 49 (2010) 919–962, <https://doi.org/10.1016/j.freeradbiomed.2010.05.009>.
- [70] J.W.J. Hamilton, J.A. Byrne, P.S.M. Dunlop, D.D. Dionysiou, M. Pelaez, K. O'Shea, D. Synnott, S.C. Pillai, Evaluating the mechanism of visible light activity for N-F-TiO₂ using photoelectrochemistry, *J. Phys. Chem. C* 118 (2014) 12206–12215, <https://doi.org/10.1021/jp4120964>.
- [71] K. Song, M. Mohseni, F. Taghipour, Mechanisms investigation on bacterial inactivation through combinations of UV wavelengths, *Water Res.* 163 (2019), 114875, <https://doi.org/10.1016/j.watres.2019.114875>.
- [72] S.E. Beck, R.A. Rodriguez, K.G. Linden, T.M. Hargy, T.C. Larason, H.B. Wright, Wavelength dependent UV inactivation and DNA damage of adenovirus as measured by cell culture infectivity and long range quantitative PCR, *Environ. Sci. Technol.* 48 (2014) 591–598, <https://doi.org/10.1021/es403850b>.
- [73] M. Cho, E.L. Cates, J.-Kim, Inactivation and surface interactions of MS-2 bacteriophage in a TiO₂ photoelectrocatalytic reactor, *Water Res.* 45 (2011) 2104–2110, <https://doi.org/10.1016/j.watres.2010.12.017>.
- [74] N. Wang, X. Zhang, B. Chen, W. Song, N.Y. Chan, H.L.W. Chan, Microfluidic photoelectrocatalytic reactors for water purification with an integrated visible-light source, *Lab Chip Miniat. Chem. Biol.* 12 (2012) 3983–3990, <https://doi.org/10.1039/c2lc40428a>.
- [75] J. Li, X. Zhang, W. Fan, M. Yao, G. Sheng, Dissolved organic matter dominating the photodegradation of free DNA bases in aquatic environments, *Water Res.* 179 (2020), 115885, <https://doi.org/10.1016/j.watres.2020.115885>.
- [76] J. Brame, M. Long, Q. Li, P. Alvarez, Trading oxidation power for efficiency: differential inhibition of photo-generated hydroxyl radicals versus singlet oxygen, *Water Res.* 60 (2014) 259–266, <https://doi.org/10.1016/j.watres.2014.05.005>.
- [77] Y. Ye, H. Bruning, W. Liu, H. Rijnaarts, D. Yntema, Effect of dissolved natural organic matter on the photocatalytic micropollutant removal performance of TiO₂ nanotube array, *J. Photochem. Photobiol. A* 371 (2019) 216–222, <https://doi.org/10.1016/j.jphotochem.2018.11.012>.
- [78] D.A. Lytle, E.W. Rice, C.H. Johnson, K.R. Fox, Electrophoretic mobilities of *Escherichia coli* O157:H7 and wild-type *Escherichia coli* strains, *Appl. Environ. Microbiol.* 65 (1999) 3222–3225, <https://doi.org/10.1128/AEM.65.7.3222-3225.1999>.